MATERIALS SCIENCE

Mechanistic basis of oxygen sensitivity in titanium

Yan Chong[1,2]*, Max Poschmann[1]*, Ruopeng Zhang[1,2]*, Shiteng Zhao[1,2], Mohammad S. Hooshmand[1], Eric Rothchild[1], David L. Olmsted[1], J. W. Morris Jr.[1], Daryl C. Chrzan[1,3†], Mark Asta[1,3†], Andrew M. Minor[1,2,3†]

One of the most potent examples of interstitial solute strengthening in metal alloys is the extreme sensitivity of titanium to small amounts of oxygen. Unfortunately, these small amounts of oxygen also lead to a markedly decreased ductility, which in turn drives the increased cost to purify titanium to avoid this oxygen poisoning effect. Here, we report a systematic study on the oxygen sensitivity of titanium that provides a clear mechanistic view of how oxygen impurities affect the mechanical properties of titanium. The increased slip planarity of Ti-O alloys is caused by an interstitial shuffling mechanism, which is sensitive to temperature, strain rate, and oxygen content and leads to the subsequent alteration of deformation twinning behavior. The insights from our experimental and computational work provide a rationale for the design of titanium alloys with increased tolerance to variations in interstitial content, with notable implications for more widespread use of titanium alloys.

INTRODUCTION

Titanium alloys have a number of highly desirable properties, including excellent corrosion resistance and high specific strength, which make them attractive structural materials for a wide range of commercial applications. Interstitial atoms, either intentionally or naturally incorporated, have a profound influence on the mechanical properties of titanium (*1*, *2*). Among the various species of interstitial impurities used, oxygen is the most widely adopted in titanium-based alloys to harness a potent strengthening effect for different applications (*2*–*4*). An inherent challenge in expanding the use of titanium alloys even further, e.g., for lightweighting in automotive applications, is their high cost. The expense of titanium is due in part to requirements for the tight control of the content of interstitial impurities in their processing and manufacturing. These requirements originate from the strong oxygen sensitivity of mechanical properties in the hexagonal close-packed (HCP) α-titanium, especially the adverse impact on ductility and fracture toughness (*3*, *5*–*10*). For example, an increase in the oxygen concentration of ~0.2 atomic % (at %) results in a several-fold increase in yield strength but even larger decrease in ductility and toughness (*6*, *7*, *11*). Despite the well-documented embrittlement effects of interstitial impurities in α-Ti (*5*, *11*, *12*), the mechanistic origin of this anomalous oxygen sensitivity upon the mechanical properties has not been clearly understood, limiting efforts in alloy design and processing strategies.

It has been documented that a "wavy-to-planar" transition of dislocation arrangements occurs with increasing oxygen content in titanium (*9*). At the microscopic level, planar slip is characterized by a more organized dislocation structure localized to a region of confined planes, while wavy slip is characterized by a more evenly distributed and multidirectional dislocation configuration. The formation of planar slip has been reported to impair various mechanical properties of α-Ti, including formability (*3*), fracture toughness (*13*), and strain-hardening ability (*5*). A wavy-to-planar transition has also been observed in the substitutional Ti-Al alloys, where the transition is hypothesized as a consequence of the chemical short-range ordering (SRO) of aluminum atoms (*13*–*15*). In Ti-Al alloys, the aluminum solutes are substitutional, and therefore the leading dislocation results in a disruption of SRO and successive dislocation motion on a "softened" glide plane. This theory is corroborated via indirect evidence, such as leading dislocations pairs resulting from the creation of a diffuse antiphase boundary (DAPB) (*16*–*18*) as well as direct characterization of the SRO structures using neutron diffraction (*19*) and energy-filtered transmission electron microscopy (TEM) (*20*). Analogously, it has been hypothesized that the formation of SRO in Ti-O alloys could be responsible for the propensity of planar dislocation slip at higher oxygen concentrations (*9*). However, the much lower concentration of solute atoms in Ti-O alloys as compared with Ti-Al alloys casts doubt on the two situations sharing the same mechanistic origin.

In the current study, we conducted a systematic multiscale investigation of the mechanical properties and deformation microstructures with regard to interstitial concentration, strain rate, and deformation temperature, aiming to reveal the nature of slip planarity associated with higher oxygen contents. Combined with the pronounced evidence of the detrimental propensity of {11-24} twinning activities, we find that the marked oxygen sensitivity in titanium can be attributed to the transitions in both dislocation behavior and twinning activity. The atomistic origin of the transitions is discussed in light of density functional theory (DFT) and molecular dynamics (MD) simulations, providing insight into the design of interstitial-tolerant titanium alloys.

RESULTS AND DISCUSSION

Mechanical properties and fracture mode

The mechanical behavior of three model alloys, namely, pure Ti [0.05 weight % (wt %) (0.15 at %) oxygen], Ti-0.1O [0.10 wt % (0.31 at %) oxygen], and Ti-0.3O [0.30 wt % (0.88 at %) oxygen], was assessed at high temperature (~500 K), room temperature (~300 K), and cryogenic temperature (~100 K) via uniaxial tensile tests with a strain rate of 10^{-3} s^{-1}. Representative engineering stress-strain curves for the two lower temperature regimes are plotted in Fig. 1A. As demonstrated in the plots, a slight variation of the oxygen

[1]Department of Materials Science and Engineering, University of California, Berkeley, Berkeley, CA 94720, USA. [2]National Center for Electron Microscopy, Molecular Foundry, Lawrence Berkeley National Laboratory, Berkeley, CA 94720, USA. [3]Materials Sciences Division, Lawrence Berkeley National Laboratory, Berkeley, CA 94720, USA.
*These authors contributed equally to this work.
†Corresponding author. Email: aminor@berkeley.edu (A.M.M.); mdasta@berkeley.edu (M.A.); dcchrzan@berkeley.edu (D.C.C.)

content resulted in marked changes to the mechanical properties of Ti-O alloys at both room and cryogenic temperatures. Specifically, at room temperature (red lines in Fig. 1A), an increase in oxygen content (from 0.05 to 0.30 wt %) led to an increase in the yield strength of Ti-O alloys from 156 to 472 MPa, at the notable cost of ductility (total elongation decreased from 48 to 16%). In comparison, the oxygen dependence of the mechanical properties of Ti-O alloys at cryogenic temperature was even more acute (blue lines in Fig. 1A). By lowering the deformation temperature, a simultaneous improvement of yield strength and ductility was identified in pure Ti compared with its room temperature counterpart. A similar phenomenon was also found in Ti-0.1O alloy. In Ti-0.3O alloy, however, despite an impressive yield strength of ~1 GPa, the material exhibited a premature fracture shortly after yielding, with a total elongation of only ~4% obtained. The catastrophic failure of Ti-0.3O alloy at low temperature is emblematic of what prevents its application at cryogenic conditions.

The marked changes in mechanical properties, particularly the tensile ductility, of Ti-O alloys with either deformation temperature or oxygen content can be seen in the evolution of strain-hardening abilities, as shown in Fig. 1B. At room temperature, the strain-hardening ability continuously decreased with increasing oxygen content, resulting in a gradual loss of ductility of Ti-O alloys. In pure Ti, a plateau stage was observed in the strain-hardening rate curves, whereas in Ti-0.1O and Ti-0.3O alloys, a monotonic decay of strain-hardening rate with ongoing strain was found. At cryogenic temperature, pure Ti and Ti-0.1O exhibited excellent and almost identical strain-hardening rates (as demonstrated by a long plateau stage in the strain-hardening rate curves), both of which were much larger than those of their room temperature counterparts. This suggests a propensity of deformation twinning at lower temperatures with low oxygen content. In the Ti-0.3O alloy, however, the strain-hardening rate quickly plunged to zero, implying a substantial transition in the deformation mechanisms triggered by both oxygen content and deformation temperature.

The potent influence of oxygen content on the mechanical properties of Ti-O alloys at different deformation temperatures is also reflected in the fracture tomography (Fig. 1, C to E). In pure Ti deformed at room temperature (Fig. 1C), the fracture surface was characterized by large dimples, which suggests an intragranular ductile fracture mode. At cryogenic temperature (Fig. 1D), the fracture mode of pure Ti was still intragranular ductile fracture, and the size of dimples became much smaller than those at room temperature. This is in a good agreement with the much higher tensile strength and even better ductility found in pure Ti deformed at cryogenic temperature than at room temperature. On the other hand, in Ti-0.3O deformed at cryogenic temperature (Fig. 1E), the fracture mode was completely changed, and a clear brittle intergranular fracture morphology together with a few cleavage features was observed. This brittle fracture mode suggests a transition to a different dominant deformation mechanism.

Dislocation activity: Wavy slip versus planar slip

The transition in deformation mode caused by oxygen content and deformation temperature can also be seen in the morphology of dislocation structures in these alloys. The typical dislocation morphologies of Ti-O alloys, either in a wavy– or planar slip–dominant mode, were systematically investigated by interrupted tensile deformations (to a plastic strain of 4.0%) at different temperatures (500, 300, and 100 K) and strain rates (10^{-5} s^{-1}, 10^{-3} s^{-1}, 10^{-1} s^{-1}, and 2 s^{-1}). The

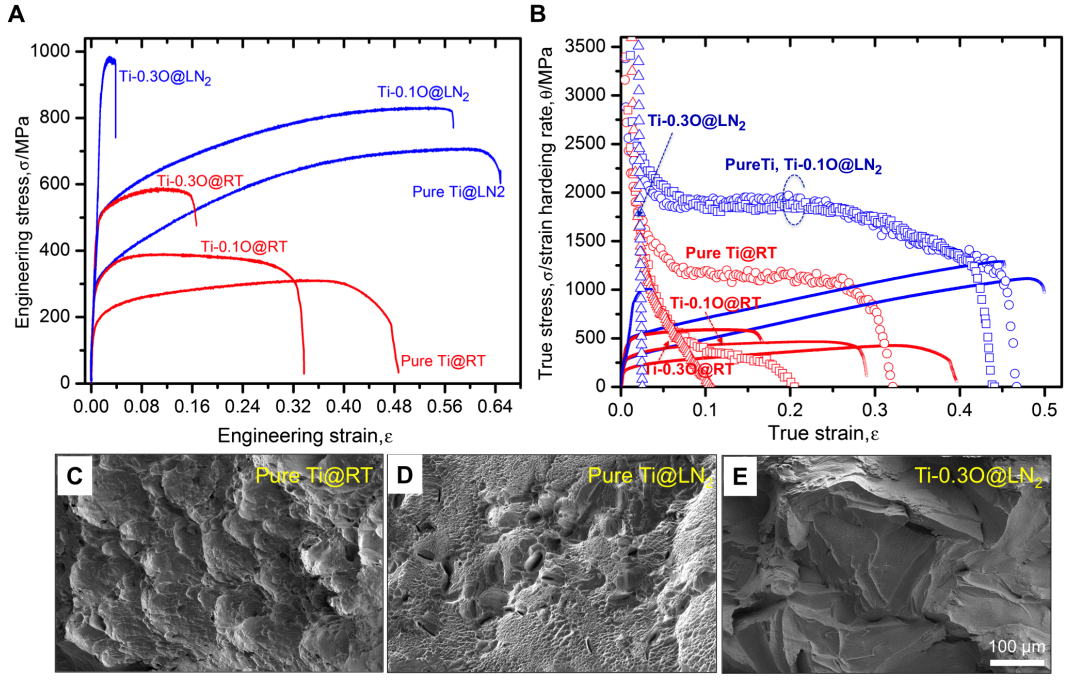

Fig. 1. Mechanical behaviors of pure Ti, Ti-0.1O, and Ti-0.3O alloys at room temperature (RT) (~300 K) and cryogenic temperature (~100 K). (**A**) Representative engineering stress-strain curves of the three alloys with a strain rate of 10^{-3} s^{-1}. (**B**) Corresponding true stress-true strain curves (solid lines) and strain hardening rate (symbols) curves of the three alloys. (**C**) Fracture tomography of pure Ti at room temperature. (**D**) Fracture tomography of pure Ti at cryogenic temperature. (**E**) Fracture tomography of Ti-0.3O at cryogenic temperature.

predominant dislocation morphology for each deformation condition was determined by investigating at least 30 grains per sample. A three-dimensional (3D) diagram demonstrating the combined analysis of the temperature, strain rate, and oxygen content dependences of the dislocation morphology is shown in Fig. 2A, in which the gray and blue points represented wavy slip–dominant and planar slip–dominant conditions, respectively. TEM images showing the representative dislocation morphologies with regard to strain rate, oxygen concentration, and deformation temperature for all of these data points are shown in figs. S1 to S3. In general, a wavy-to-planar slip transition was prone to occur with either increasing strain rate, i.e., from Fig. 2C (pure Ti, 10^{-1} s^{-1}, LN_2) to Fig. 2B (pure Ti, 2 s^{-1}, LN_2), or increasing oxygen content, i.e., from Fig. 2D (Ti-0.1O, 10^{-5} s^{-1}, LN_2) to Fig. 2E (Ti-0.3O, 10^{-5} s^{-1}, LN_2), or decreasing temperature, i.e., from Fig. 2F (Ti-0.3O, 10^{-3} s^{-1}, RT) to Fig. 2G (Ti-0.3O, 10^{-3} s^{-1}, LN_2). A clear transition boundary delineating the planar slip–dominant and wavy slip–dominant regions can be found for each oxygen content. In pure Ti (containing 0.05 wt % oxygen), the transition boundary is located at the bottom left corner of the corresponding plane in Fig. 2A, which suggests a rather rigorous requirement (extremely low deformation temperature and large strain rate) for the occurrence of planar slip at such a low oxygen content. With increasing oxygen content, however, the critical condition for the wavy-to-planar slip transition relaxes, as manifested by the transition boundary progressively shifting toward the upper right corner of the corresponding planes. It is worth noting that planar slip was actually found at room temperature in the Ti-0.3O alloy at relatively high strain rates (10^{-1} s^{-1} and 2 s^{-1}) (Fig. 2A and fig. S1), whereas planar slip in Ti-O alloys has been predominantly reported for cryogenic deformation conditions in the previous studies (*3*, *5*, *6*). Last, it should be pointed out that, by a careful $\boldsymbol{g} \cdot \boldsymbol{b}$ analysis, most of the dislocations we characterized, either in a wavy or planar slip morphology, were confirmed to be <***a***>-type dislocations, although we cannot exclude the possibility of a few <***c*** + ***a***>-type dislocations close to grain boundary areas, especially in specimens with higher oxygen content and lower deformation temperature, where large flow stresses were realized (*5*).

Despite the fact that planar slip has been frequently reported in Ti-O alloys (*3*, *5*, *9*), particularly at cryogenic deformation temperatures, the underlying mechanism has not been clear. It has been proposed that the SRO of oxygen atoms could be a possible mechanism, similar to the case of Ti-Al alloys (*13*–*15*, *20*). However, the SRO of oxygen in the Ti-O binary system with such a dilute oxygen content has never been experimentally verified. The diffuse DAPB energy

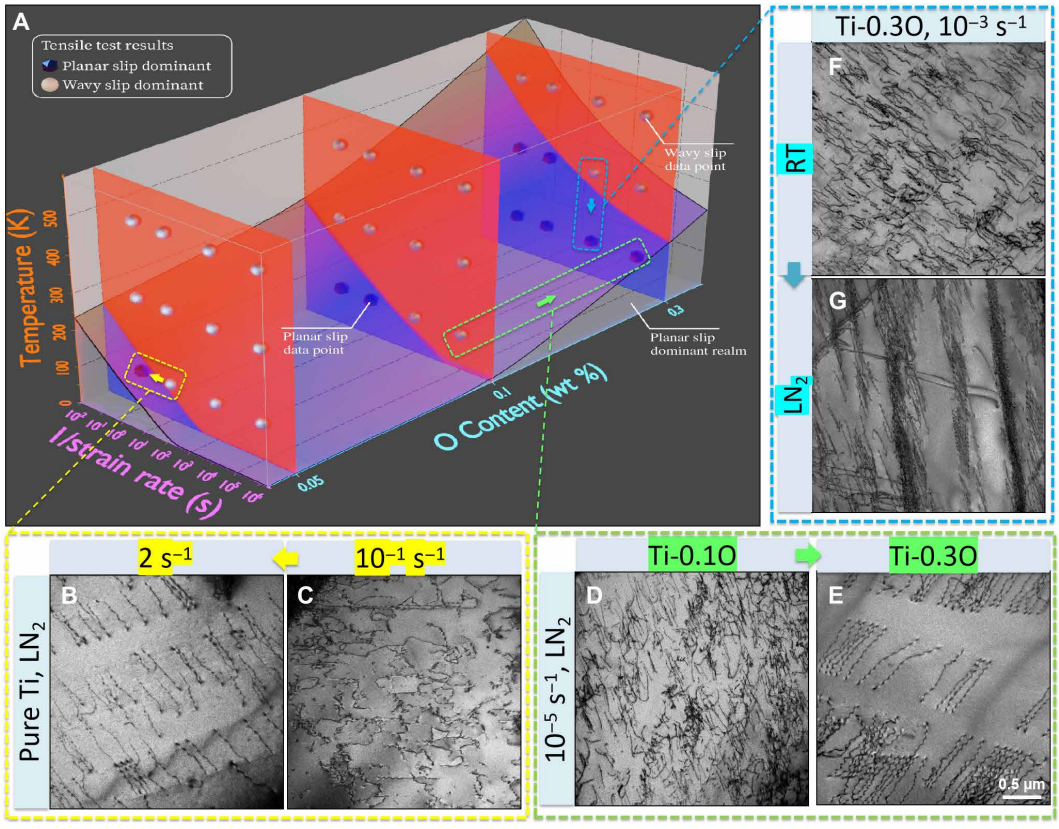

Fig. 2. Comparison of typical dislocation morphologies (wavy or planar slip dominant) in Ti-O alloys after interrupted tensile deformations at different temperatures (500, 300, and 100 K) and strain rates ($10^{-5}s^{-1}$, $10^{-3}s^{-1}$, $10^{-1}s^{-1}$, and 2 s^{-1}). The tensile strain was 4.0% for all the microstructures. (**A**) 3D diagram demonstrating the combined analysis of temperature, strain rate, and oxygen content dependences of dislocation morphologies in Ti-O alloys. A general tendency of wavy-to-planar slip transition occurred with either increasing strain rate, i.e., from (**C**) (pure Ti, 10^{-1} s^{-1}, LN_2) to (**B**) (pure Ti, 2 s^{-1}, LN_2), or increasing oxygen content, i.e., from (**D**) (Ti-0.1O, 10^{-5} s^{-1}, LN_2) to (**E**) (Ti-0.3O, 10^{-5} s^{-1}, LN_2), or decreasing temperature, i.e., from (**F**) (Ti-0.3O, 10^{-3} s^{-1}, RT) to (**G**) (Ti-0.3O, 10^{-3} s^{-1}, LN_2). The transition boundary delineating wavy slip–dominant and planar slip–dominant regions gradually shifted toward a higher temperature and lower strain rate direction with increasing oxygen content.

assuming equilibrium SRO in Ti-0.3O alloy was calculated using the framework of first principles cluster expansion methods and Monte Carlo simulations. As summarized in the Supplementary Materials, these calculations established that the DAPB energies in the Ti-0.3O alloy are two orders of magnitude smaller than those for Ti-Al alloys (*21*). The DAPB energies of Ti-0.3O alloy calculated in this work are even smaller than those computed for high-temperature processed and rapidly quenched Ti-Al alloys where planar slip was not observed experimentally (*21*). In addition, for the Ti–6 wt % Al alloy, the planar slip was caused by slip plane softening due to the destruction of SRO by dislocation slip. Therefore, the occurrence of planar slip was confirmed to be temperature and strain rate independent (as shown in fig. S4). This is in sharp contrast to the temperature and strain rate dependences of planar slip we found in Ti-O alloys. It is also worth noting that the SRO-induced planar slip would usually leave a residual strain field caused by the destruction of SRO on the glide plane (*18*, *20*). No similar observation has ever been reported in Ti-O alloys. Because of these factors, it is clear that there must be a different origin to the evolution of planar slip in Ti-O alloys other than the destruction of SRO.

Interstitial shuffling mechanism for the Ti-O system

On the basis of first principles DFT calculations, we propose here a novel interstitial shuffling mechanism (ISM) to account for the temperature and strain rate dependences of the wavy-to-planar slip transition in Ti-O alloys. In the ISM model, the competition between two processes involving the motion of oxygen atoms between different interstitial sites (either the octahedral or hexahedral sites) determines the dislocation morphology of Ti-O alloys. The geometry sizes characterized by the nearest-neighbor distance after relaxation were 2.09 and 1.92 Å for the octahedral site and hexahedral site, respectively (*22*). To begin the process, oxygen atoms that are initially found at the more stable octahedral sites are shuffled by <***a***>-type screw dislocations moving on prismatic planes to hexahedral sites, where they present less resistance to dislocation motion. This creates a slip plane softening effect that results in planar slip behavior. Following the initial slip plane softening, thermal fluctuations cause some of the oxygen atoms that have been shuffled by dislocations into the high-energy hexahedral sites to hop back into the stable octahedral position. This hexahedral-to-octahedral hopping increases the resistance to slip in a given slip band, and therefore decreases the tendency for planar dislocation slip. As a result, the interplay between the two processes determines whether planar slip will occur, which in turn produces the temperature and strain rate dependences of wavy-to-planar slip transition in Ti-O alloys that we have shown experimentally. Higher temperature would promote more hexahedral-to-octahedral hopping, while lower strain rate would retard the interstitial shuffling rate, making wavy slip dominate at these deformation conditions. On the other hand, at lower temperatures and larger strain rates, the oxygen hopping would be largely suppressed while the shuffling process occurs regardless of dislocation motion, which makes planar slip easier at these deformation conditions.

Generalized stacking fault (GSF) energies, obtained by first principles DFT calculations (see the "Computational method" section for more details), provide computational evidence for the slip plane softening effect associated with the shuffling process (Fig. 3). In these calculations, we used a modified GSF method in which steps along the direction of the Burgers vector through the stacking fault energy surface were simulated, with relaxations permitted perpendicular

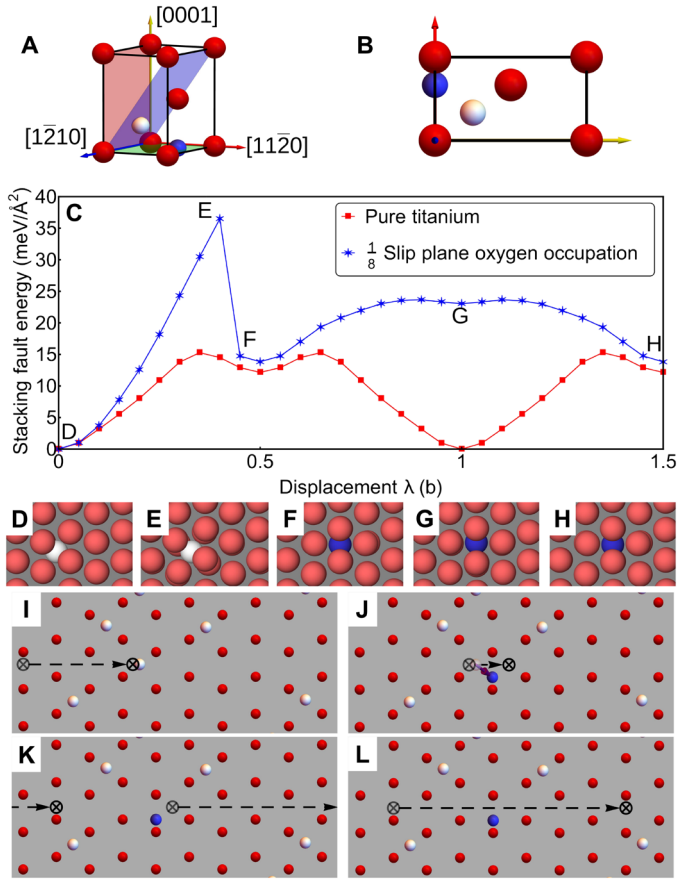

Fig. 3. Schematic illustration of ISM of slip plane softening. (**A**) HCP lattice with octahedral (white) and hexahedral (blue) sites, and prismatic, pyramidal, and basal planes (red, blue, and green). (**B**) Orientation for the steps of dislocation slip shown in (I) to (L). (**C**) Modified GSF energy on the prismatic plane calculated with DFT. (**D**) to (**H**) show oxygen position for selected steps, starting from octahedral (D). (E) shows the distorted octahedral site at the maximum in energy. In steps (F) and (H), the oxygen is in an octahedral site formed at the stacking fault. (G) shows the hexahedral site. (**I**) to (**L**) demonstrate the key steps in the ISM model. In (I), the first dislocation (cross symbol) on a prismatic plane encounters an octahedral oxygen and slip is resisted. It eventually overcomes this obstacle and shuffles the oxygen to the hexahedral site (J). The dislocation continues slipping, and subsequent dislocations follow behind (K). These dislocations see a reduced barrier from the hexahedral oxygen and thus easily slip on this plane (L).

to the Burgers vector. The lowest-energy path across the associated γ-surface in the direction of a dislocation Burgers vector is related to the energy barrier for slip of that dislocation. The modified GSF energies on the {10-10} prismatic plane for pure Ti and Ti with one in eight octahedral sites on the slip plane occupied by oxygen impurities are shown in Fig. 3C. The prismatic plane is of interest because slip of <***a***>-type screw dislocations on this plane represents the most active dislocation slip system in commercial purity (CP)–Ti.

For pure Ti, the GSF energy increases rapidly up to a shift of λ = 0.35 (i.e., 0.35 of the Burgers vector), and then decreases to a local minimum at λ = 0.5. The barrier to complete the slip (i.e., from λ = 0.5 to 1) is symmetric. In comparison, for the results along the same slip path in the system containing oxygen, the modified GSF energy is seen to increase more sharply during the early stages of slip, until λ = 0.45 when a sharp drop in the energy occurs. This energy drop

is associated with the shuffling of the oxygen interstitial out of the low-energy octahedral site, to a site within the basal plane that is associated with the so-called hexahedral position (*23*) in the undeformed HCP structure. In the HCP structure, the oxygen atom has a much higher energy in the hexahedral site than it does in the more open octahedral site. However, the octahedral site becomes increasingly compressed during slip, while the hexahedral site becomes more "open" along the shear path. Although the oxygen shuffle and associated GSF energy drop were previously reported (*24*, *25*), the most interesting finding of the present study is that when slip is completed ($\lambda = 1$), the oxygen interstitial remains in the basal plane site (the barrier to return to the octahedral site is 890 meV), and the barrier to further slip is substantially reduced. Specifically, consider two complete slip paths for the oxygen-containing system shown in Fig. 3C: $\lambda = 0 \rightarrow 1$ and $\lambda = 0.5 \rightarrow 1.5$. For both, the energy barrier to slip corresponds to the difference between the lowest and highest GSF energies along the path. In the first slip event, the barrier is 36.5 meV/Å^2 [which matches nudged elastic band (NEB) calculations by Kwasniak and co-workers closely (*25*)], while in the second, it is reduced to 9.8 meV/Å^2. Because the basal plane site is part-way out of the slip plane, the steric hindrance to slip is notably reduced by the shuffle of the oxygen atom into this site. The GSF calculations thus support the ISM for slip plane softening illustrated in Fig. 3 (I to L). The first slip event on a given slip plane leads to displacement of oxygen impurities to the basal plane site (Fig. 3, I and J). The displaced oxygen atoms remain in these positions, which leaves the barrier to further slip reduced (Fig. 3, K and L).

Further evidence for the reduced barrier to slip presented by the oxygen in the hexahedral site rather than in the octahedral site has been provided by dislocation pinning calculations performed using the modified embedded atom method (MEAM) (*26*). By calculating the maximum bowing angles of dislocations pinned at oxygen interstitials, we found that the pinning strength of octahedral oxygen is approximately 55% higher than that of hexahedral oxygen. Please see Supplementary Text, table S3, and fig. S5 for more details.

Twinning activity as a function of oxygen and temperature

In addition to the dislocation activity, deformation twinning is critical for understanding the mechanical properties of Ti-O alloys, as <***a***>-type dislocation motion alone, either in the form of a wavy slip or a planar slip, is not sufficient to accommodate an arbitrary plastic deformation. Deformation twinning in titanium provides the necessary path to accommodate deformation along the ***c*** axis. Twinning is the origin of excellent mechanical properties observed at cryogenic temperature in titanium alloys, where dislocation activities become difficult. To date, there have been four common deformation twinning modes reported in titanium, including two tension twins (T1 {10-12} <-1011> and T2 {11-21} <−1-126>) and two compression twins (C1 {11-22} < 11-2-3 > and C2 {10-11} < 10-1-2>) (*27*–*30*). At room temperature, T1 is the predominant twinning mode due to its low shear strain and simple shuffling mechanism (*28*). An overview of the twinning behavior as a function of oxygen content and temperature is shown in Fig. 4. In the microstructure of tensile fractured pure Ti at room temperature (Fig. 4A), large lenticular shaped twins were commonly observed with the appearance of secondary twins inside the primary twins. With increasing oxygen content (Fig. 4, B and C), however, the twin fractions at room temperature were continuously reduced to the point that in the Ti-0.3O alloy no appreciable twins

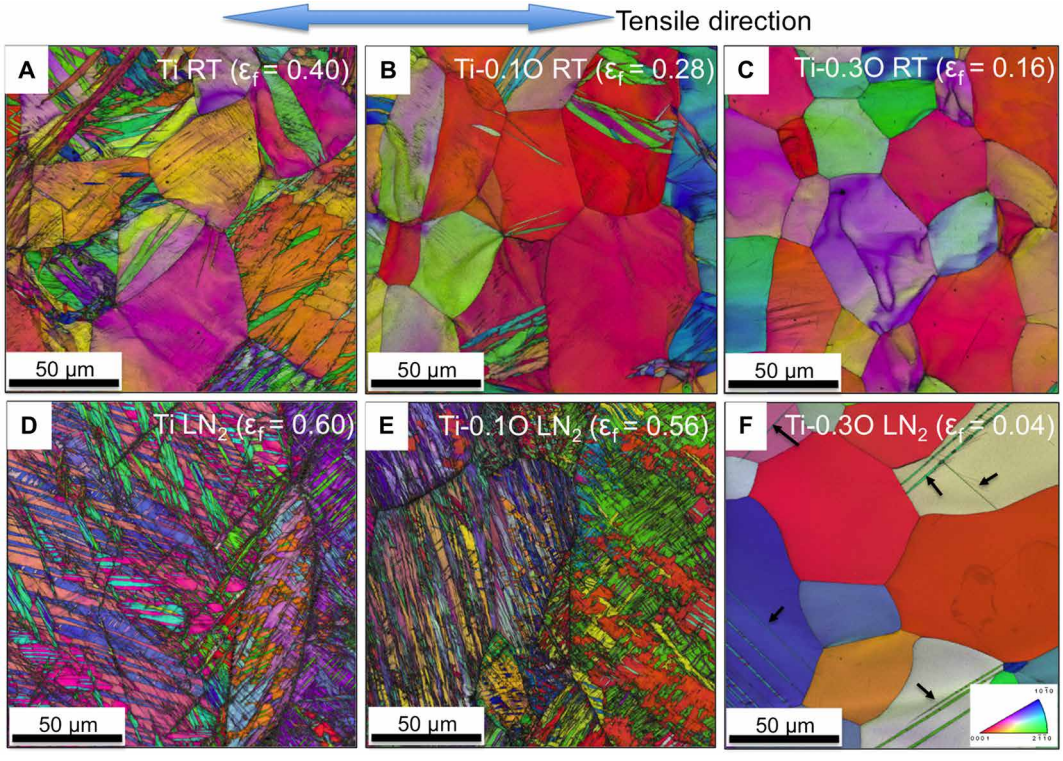

Fig. 4. Inverse pole figure (IPF) + image quality (IQ) maps of Ti-O alloys after tensile fractured at room temperature (RT) and cryogenic temperature (LN_2), with a strain rate of $10^{-3}s^{-1}$. (**A**) Pure Ti, RT, and fracture strain: 0.40. (**B**) Ti-0.10, RT, and fracture strain: 0.28. (**C**) Ti-0.3O, RT, and fracture strain: 0.16. (**D**) Pure Ti, LN_2, and fracture strain: 0.60. (**E**) Ti-0.1O, LN_2, and fracture strain: 0.56. (**F**) Ti-0.3O, LN_2, and fracture strain: 0.04. The tensile direction is horizontal for all the microstructures.

could be detected at room temperature. The types of deformation twins (as shown in fig. S6) in pure Ti and Ti-0.1O at room temperature were confirmed to be either T1 (in red color) or C1 twins (in green color), which agrees well with the previous literature on titanium (*28*–*30*).

At cryogenic temperature, the twinning activity in pure Ti was substantially enhanced (Fig. 4D), leading to the subdivision of the original grains by a high density of primary and secondary twins with a much smaller thickness (see fig. S7). As a result of the extensive deformation twinning, pure Ti exhibited a much higher strain hardening rate and total elongation at cryogenic temperature than at room temperature. The enhanced twinning activity in pure Ti at cryogenic temperature can be ascribed to a larger internal stress level, whereas the critical resolved shear stress for twin nucleation is essentially temperature insensitive. Unlike the suppressed twinning activity found at room temperature, at cryogenic temperature, the Ti-0.1O alloy also showed an almost fully twinned microstructure after tensile fracture (Fig. 4E).

Unexpectedly, we found that the Ti-0.3O alloy did show appreciable twins at cryogenic temperature (Fig. 4F), even though the fracture strain (~4%) was much smaller than that of Ti-0.3O alloy (~16%) at room temperature. These nano-sized twins, however, did not give rise to an improvement in the ductility of Ti-0.3O alloy at cryogenic temperature as expected. Instead, the tensile specimen showed a premature fracture shortly after yielding, contrary to the case at room temperature, in which a reasonable ductility was maintained without the contribution of twinning. These nano-sized twins found in the tensile fractured Ti-0.3O at cryogenic temperature were universally confirmed to be the {11-24} twin with a characteristic misorientation angle of 77° across the plane normal of <01-10> (see fig. S6F). This type of twin has only been occasionally reported in CP titanium deformed at some extreme conditions, i.e., fast strain rates (*31*, *32*) such as ballistic impact testing at 10^3 s^{-1} (*32*), or cryogenic temperatures (*33*–*35*). In most cases, the fraction of the {11-24} twin type was rather limited, and it tended to occur in CP titanium with relatively high oxygen contents (*32*–*35*). As shown in Fig. 5, most of the twins activated in this sample were confirmed to be the {11-24} twin, despite the existence of a few T1 and C1 twins (Fig. 5, B and G). To our knowledge, such a predominance of {11-24} twinning over conventional tension and compression twins (as shown in fig. S6F and Fig. 5B) has never been reported in titanium at any deformation condition before. In the corresponding misorientation angle profile (Fig. 5E), a clear peak was observed around 77°, which is characteristic of the {11-24} twin. In optical microscopy (Fig. 5A), several microcracks were observed, most of which were located along the grain boundaries (as indicated by yellow arrows). These microcracks once formed, could easily propagate along the grain boundaries, and considering the relatively large grain size of Ti-O alloys, a premature fracture shortly after yielding would be expected. This is also consistent with the intergranular fracture morphology found in Ti-0.3O alloy at cryogenic temperature (Fig. 1E). Observation of these microcracks leads to the notable finding that most are located at the intersection points where the {11-24} twins' propagation was blocked at grain boundaries. One typical example of this interaction is shown in Fig. 5 (C and D), where the microcracks connecting to {11-24} twins were marked by yellow arrows. A TEM specimen was prepared from one of the {11-24} twins connecting to microcracks (marked by the orange rectangle in Fig. 5B) by a lift-out method using the focused ion beam (FIB). A high-resolution TEM (HRTEM) image (zone axis of [-5143]) showing the lattice structure at the twin/matrix interface is given in Fig. 5F, in which a large lattice distortion was observed around the interface. This HRTEM image also displayed for the first time the detailed lattice structure around this unusual twin in titanium.

To further understand the anomalous behavior of {11-24} twins, we studied the interaction between the oxygen and twin boundaries (TB) using atomistic simulations. Previous experimental (*5*) and computational (*36*, *37*) studies showed that oxygen solutes tend to suppress the most commonly observed {10-12} twins at low temperatures in Ti. This suppression has been attributed to the attractive binding between oxygen and the TB, which results in pinning and, therefore, slower growth of {10-12} TB (*36*, *37*). Here, we simulated {10-11}, {10-12}, {11-21}, {11-22}, and {11-24} TB and computed the interaction energy of oxygen with each boundary using the MEAM potential referenced above calculations at 0 K temperature (for details of the simulations, refer to the Supplementary Materials). We find that while oxygen is attracted to the {10-11}, {10-12}, and {11-21} TB, it is not favorable for oxygen to segregate to the {11-22} and {11-24} TB, and therefore, oxygen prefers to stay in the bulk. This finding is in agreement with the predominance of {11-24} and {11-22} twins observed experimentally at higher–oxygen concentration samples (Fig. 5). In other words, the lack of attraction of O to the {11-24} and {11-22} twins means that at high stresses, these twin types can grow at high oxygen concentrations unlike the other more commonly observed twin modes.

Summary and implications

Taking into account the systematic influence of oxygen on the dislocation morphology and twinning fraction as well as twinning type, it is possible to present a mechanistic picture of the oxygen sensitivity of the mechanical properties in titanium. We can attribute the origin of temperature, strain rate, and oxygen content sensitivity of slip planarity in Ti-O alloys to the motion of oxygen atoms rather than to the presence of SRO. The ISM model provides an explanation of the observed temperature and strain rate sensitivity of planar slip in Ti-O alloys, which involves the competing effects of interstitial oxygen shuffle by dislocations and subsequent hopping of metastable interstitial oxygen to the stable site. This model may also apply to other alloy systems containing interstitial solutes that interact strongly with relevant dislocations. The increase in planar slip and suppression of deformation twinning with increasing oxygen content leads to a lack of strain-hardening ability in Ti-O alloys. In the extreme case of high oxygen, low temperature, and, therefore, high flow stress, the Ti-0.3O alloy generates an uncommon {11-24} twin type that leads to intergranular cracking and explains the origin of oxygen poisoning effect in cryogenic conditions. This result highlights the need for further theoretical and simulation work to understand the fundamental mechanisms for the abnormally enhanced {11-24} twin by considering the interactions between oxygen atoms and TB.

Our results suggest that alloy design strategies that interrupt the interstitial shuffling process (e.g., increasing the energy of the metastable hexahedral sites by tuning the lattice parameters via substitutional alloying) may notably increase the interstitial tolerance of titanium alloys. In addition, methods to either promote conventional deformation twinning or suppress {11-24} twinning should be applied if applications at cryogenic temperature are desired. In contrast to SRO-induced deformation localization that is found in Ti-Al systems (*16*), the strain rate sensitivity of planar slip in

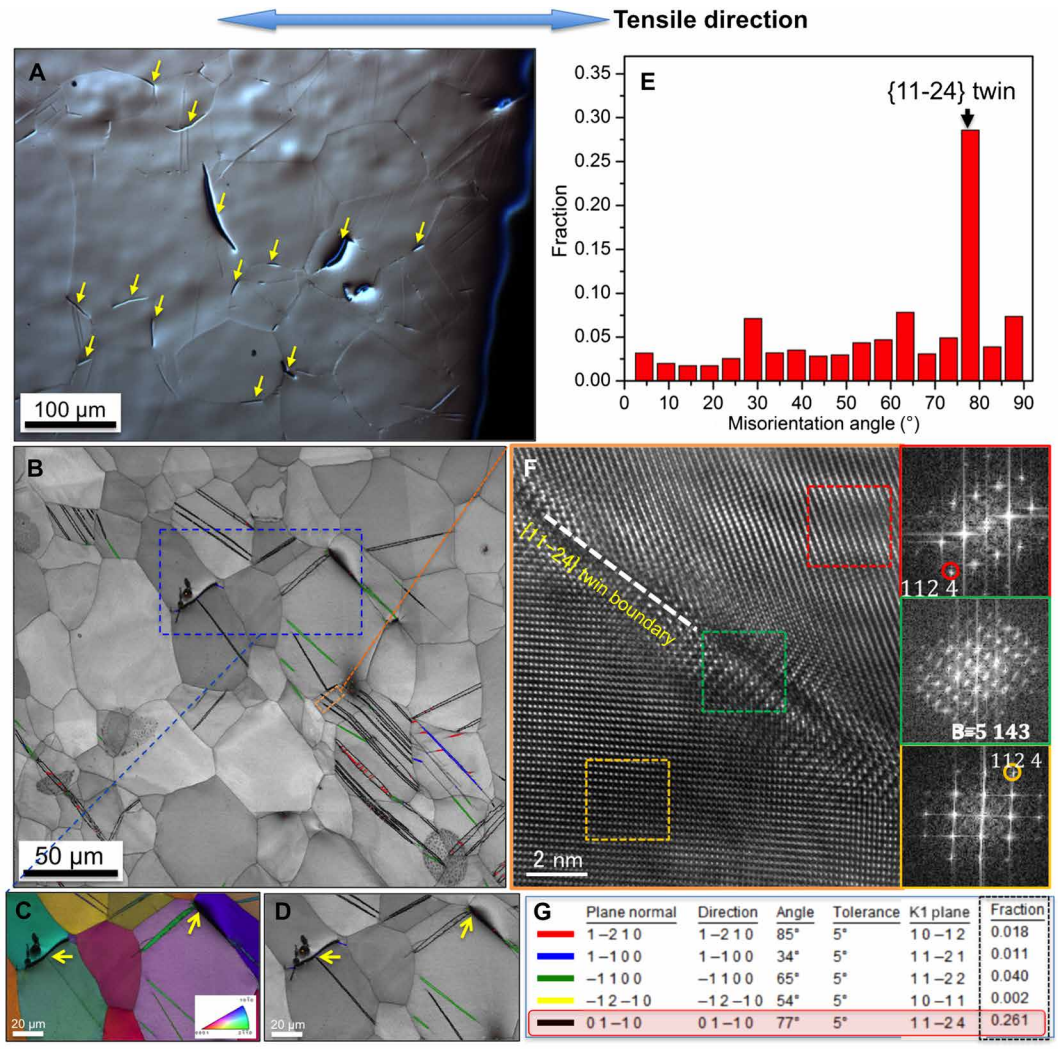

Fig. 5. Characterization of Ti-0.3O alloy after tensile fractured at cryogenic temperature. (**A**) Optical microscopy of the area near fracture surface, in which several microcracks (as indicated by yellow arrows) were observed along the grain boundaries. (**B**) Twin boundary map showing the types of twins near the fracture surface [according to the colors shown in (G)]. (**C**) and (**D**) are the IPF map and twin boundary map showing one typical example of microcracks forming at the points where {11-24} twins were blocked at the grain boundaries. (**E**) The misorientation angle profile, in which an evident peak was found at 77°, confirming the predominance of {11-24} twins in Ti-0.3O deformed at cryogenic temperature. (**F**) The HRTEM image (from a zone axis of [-5143]) of one {11-24} twin lifted out from the rectangle area in (B) by the focused ion beam (FIB) method. (**G**) The colors used in panels B and D.

Ti-O alloys also implies that the strengthening effect provided by interstitial atoms is of great benefit for creep performance (low strain rates) without any accompanying sacrifice in ductility.

MATERIALS AND METHODS

Materials processing and mechanical property testing

Three Ti ingots with different oxygen contents (0.05, 0.10, and 0.30 wt %) were provided by TIMET, UK, which will be referred to as pure Ti, Ti-0.1O, and Ti-0.3O hereafter for simplicity. The detailed chemical compositions of the three ingots are given in table S1. The ingots were argon arc double melted and then forged into square bars at 1125°C before water quenching. The bars were then rolled at 900°C and annealed at 800°C for 1 hour. The as-annealed materials were characterized by a fully equiaxed microstructure with an average grain size of ~60 μm and nearly free of dislocations. They will be used as the starting microstructure for subsequent mechanical property testing and microstructure characterization.

Dog bone–shaped microtensile specimens with a gauge length of 5.0 mm, width of 1.6 mm, and thickness of 0.8 mm were prepared from the as-annealed materials by electrical discharge machining. Uniaxial tensile tests were performed on an MTS criterion (model 43) system with an initial strain rate of 10^{-3} s^{-1} at both room temperature (~300 K) and cryogenic temperature (~100 K). For the room temperature tensile tests, tensile stresses were provided by the MTS system, while the tensile strains were accurately measured by a digital image correlation (DIC) method. Surfaces of the microtensile specimens were sprayed with white and black contrast particles, which served as markers for the DIC analysis. During the tensile tests, images of the microtensile specimens were captured by a charge-coupled device (CCD) camera, which were later analyzed by the Vic-2D commercial software. The accurate plastic strain (von Mises strain)

of the tensile specimen can be obtained by tracking the positions of markers. For the cryogenic temperature tensile tests, a special plastic container was designed, which allowed a full immersion of both the tensile specimens and tensile jigs in the liquid nitrogen throughout the whole tensile test process. The tensile specimens were held in liquid nitrogen for 10 min to homogenize the temperature before tensile tests. The tensile strains given by the MTS system were correlated using the room temperature strain data (obtained by the DIC method), assuming an unchanged Young's modulus at the two testing temperatures. For each alloy, at least three specimens were tested at each deformation temperature to confirm the reproductivity of mechanical properties.

For dislocation morphology analysis, another set of interrupted tensile deformation experiments were carried out at three different temperatures (500, 300, and 100 K) and four different strain rates [10^{-5} s^{-1}, 10^{-3} s^{-1}, 10^{-1} s^{-1}, and 2 s^{-1} (the maximum strain rate that was achieved in the MTS system for the specimen geometry used in this study)]. All the specimens were tensile deformed to a plastic strain of 4.0% and then unloaded for subsequent microstructure characterization. In addition, a Ti–6 wt % Al alloy with promoted SRO (by aging at 420°C for 120 hours) was also tensile deformed at some of the abovementioned deformation conditions. Details of the processing history of the Ti–6 wt % Al alloy as well as the direct imaging of SRO can be found elsewhere (*20*). For dislocation morphology analysis, at least 30 grains were checked for each sample. Emphasis was laid on dislocations inside the grains, while those near the grain boundary areas were avoided.

Sample preparation and characterization method

The surfaces of tensile fractured specimens were ground and mechanically polished with silicon carbide abrasive paper (P160 to P4000). Final electropolishing in a solution of 6% perchloric acid and 94% methanol was conducted at −40°C using a voltage of ~30 V for 30 s. Electron backscattered diffraction (EBSD) characterizations were carried out at areas close to the lateral fracture surfaces, using the TSL system attached to a field emission gun scanning electron microscopy (SEM) FEI Strata 235, operated at an accelerating voltage of 20 kV. The collected data were analyzed using the TSL-OIM software. SEM characterizations perpendicular to the tensile fracture surfaces were also conducted using the same facility.

Samples for TEM investigations were prepared from the specimens after interrupted tensile deformation. The deformed specimens were first mechanically polished to a thickness of ~100 μm. The thickness was further reduced by a standard twin-jet electropolishing method using a Fischione (modal 110) device at −40°C using a voltage of ~30 V, in a solution of 6% perchloric acid and 94% methanol. TEM characterization of dislocation morphologies was conducted on JEOL 3010 TEM operated at 300 kV. For characterizing the {11-24} twin found in the Ti-0.3O alloy fractured at cryogenic temperature, the TEM sample was prepared by a lift-out method from the EBSD scanned area, using an FEI Helios G4 UX dual beam FIB. HRTEM characterization of the {11-24} twin was carried out on FEI TitanX 60-300 TEM operated at 300 kV.

Computational method

Modified GSF calculations

In GSF energy calculations (*38*), a continuum of possible stacking faults is considered, and an energy surface representing these is formed. The method presented here is modified to accommodate investigation of interstitial effects by performing calculations in series (with each input configuration depending on previous output) and by searching along a path in the direction of the Burgers vector through the stacking fault energy surface with relaxations permitted perpendicular to the Burgers vector. This approach allows for examination of steric interactions between oxygen interstitials and dislocation slip, isolated from dislocation core effects and without the need for expensive dislocation quadrupole configurations. It also solves the issue of where to place the oxygen interstitial that would arise if the entire stacking fault energy surface was calculated with each configuration independently initiated. In the GSF construction, a slip plane of interest is selected, and a supercell was constructed that is long (at least 30 Å) in the direction normal to this plane, with the perpendicular directions generally shorter. The supercell has periodic boundaries in the directions contained in the slip plane but is nonperiodic (using a vacuum layer of at least 15 Å in plane wave–based DFT calculations) perpendicular to the slip plane. A single oxygen atom is placed in an octahedral site on the slip plane, which is chosen to be midway up the supercell.

The calculation proceeds as follows:

(1) atom positions are fully relaxed,

(2) atoms above the slip plane are displaced by a fraction of the Burgers vector relative to those below,

(3) constrained relaxation of atomic positions,

(4) repeat (2) and (3) until slip is complete.

As the oxygen atom is on the slip plane, it is displaced by half the step size to avoid biasing its relaxation. During constrained relaxation, titanium atoms are allowed to relax within the plane normal to the Burgers vector. The reasoning behind this is allowing as much relaxation as possible most closely reflects realistic conditions. However, if atoms are allowed to relax along the Burgers vector, they may simply undo the applied slip. The oxygen atom is always permitted to relax without constraint. Lattice parameters are kept fixed with the justification that in a bulk crystal, the large undeformed volume would constrain the dimensions of the area around the dislocation or stacking fault. The modification introduced here to allow planar relaxation of the titanium atoms is an important one, as the novel findings presented below only occur if this relaxation is allowed.

The energy (E) is output after each relaxation, and the GSF energy at each step is calculated as follows

$$\mathrm{GSF}(\lambda) = \frac{E(\lambda) - E(\lambda = 0)}{A}$$

where λ is the fraction of slip along the Burgers vector and A is the slip plane area per supercell.

Dislocation calculations

Calculations on quadrupolar dislocation configurations were initialized by introducing two <***a***>-type screw dislocations with Burgers vector $\boldsymbol{a}\langle 11\text{-}\bar{2}0\rangle/3$ (of opposite sign for the two dislocations) into a pure Ti supercell of the desired size using the method of Daw (*39*) and accounting for the distortion from the dislocations as prescribed by Lehto *et al.* (*40*).

To measure dislocation bowing angles, we constructed six configurations using the method of Cai *et al.* (*41*) modified to include homogeneously strained layers at the surfaces to suppress the image forces on the dislocation. The supercells contained 1,806,336, 3,612,672, and 5,419,008 titanium atoms and 1 oxygen atom placed in the slip plane of the dislocation [one case of octahedral placement and one of oxygen placement in the basal plane site (hexahedral) were considered

for each supercell size]. The three supercell sizes differed only in the length along the dislocation line direction (which corresponded to the length between oxygen pinning sites) and were 281, 563, and 845 Å. We performed constant strain rate MD simulations for each simulation cell at zero temperature, with a strain rate of 8.17×10^6 s^{-1}.

Computational settings

All DFT calculations were performed using the Vienna ab initio simulation package (*42*). The projector-augmented wave (*43*) method was used, and the calculations were not spin polarized. The titanium potential of the Perdew-Burke-Ernzerhof (PBE) (*44*) form of the general gradient approximation (GGA) including the $3d^2 4s^2 3p^6$ electrons as valence was used for all following DFT calculations. The PBE potential for oxygen of intermediate hardness was used. The second-order Methfessel-Paxton smearing scheme (*45*) was used with a smearing width of 0.2 eV. The cutoff energy for the plane wave basis was 400 eV for modified GSF calculations involving only titanium, 520 eV for modified GSF calculations, which included oxygen atoms, and 600 eV for calculations including dislocations. Electronic structure self-consistency loops were terminated at an energy tolerance of 10^{-5} eV, and ionic relaxation was terminated at an energy tolerance of 10^{-4} eV for modified GSF calculations and force tolerance 0.02 eV/Å for dislocation calculations. K-point meshes for modified GSF calculations were generated using the k-point grid server (*46*) with minimum real-space grid distance of 37 Å, and for dislocation calculations, a $1 \times 1 \times 5$ Γ-centered grid was used. These parameters have been demonstrated to be sufficient to capture the relevant information about these dislocation core structures (*47*). The short-range order calculations used the same potential as above. The runs for the force constant, Kanzaki forces, elastic modulus, and the lattice expansion coefficients used an energy cutoff for the plane waves of 600 eV and converged the forces to 0.001 eV/Å. The runs for the cluster expansion, where only the energy is relevant, used an energy cutoff of 520 eV and converged the forces to 0.015 eV/Å. None of the simulations were spin polarized.

Classical potential calculations were performed using the large-scale atomic/molecular massively parallel simulator (LAMMPS) (*48*). The MEAM (*26*) potential of Hennig *et al.* (*49*) was used for pure Ti calculations, as well as the closely related potential for Ti-O systems by Zhang *et al.* (*50*). This potential has been shown to represent the relative energies of the important interstitial sites for oxygen in titanium (octahedral, hexahedral, and crowdion) accurately, as well as the barriers between these sites (*50*). Relaxation was performed at zero temperature and terminated when the norm of the forces on all atoms was less than 10^{-4} eV/Å.

SUPPLEMENTARY MATERIALS

Supplementary Material for this article is available at http://advances.sciencemag.org/cgi/content/full/6/43/eabc4060/DC1

REFERENCES AND NOTES

1. D. Banerjee, J. C. Williams, Perspectives on titanium science and technology. *Acta Mater.* **61**, 844–879 (2013).
2. G. Lütjering, J. C. Williams, *Titanium* (Springer, 2003).
3. J. R. Davis, *Metals Handbook* (1998).
4. M. Peters, C. Leyens, *Titanium and Titanium Alloys - Fundamentals and Applications* (Wiley VCH, 2003), vol. 1.
5. H. Conrad, Effect of interstitial solutes on the strength and ductility of titanium. *Prog. Mater. Sci.* **26**, 123–403 (1981).
6. M. L. Wasz, F. R. Brotzen, R. B. McLellan, A. J. Griffin, Effect of oxygen and hydrogen on mechanical properties of commercial purity titanium. *Int. Mater. Rev.* **41**, 1–12 (1996).
7. P. A. Russo, S. R. Seagle, *ASTM Special Technical Publication* (1984), pp. 99–112.
8. Q. Yu, L. Qi, T. Tsuru, R. Traylor, D. Rugg, J. W. Morris Jr., M. Asta, D. C. Chrzan, A. M. Minor, Origin of dramatic oxygen solute strengthening effect in titanium. *Science* **347**, 635–639 (2015).
9. J. C. Williams, A. W. Sommer, P. P. Tung, The influence of oxygen concentration on the internal stress and dislocation arrangements in α titanium. *Metall. Mater. Trans. B* **3**, 2979–2984 (1972).
10. T. A. Parthasarathy, W. J. Porter, S. Boone, R. John, P. Martin, Life prediction under tension of titanium alloys that develop an oxygenated brittle case during use. *Scr. Mater.* **65**, 420–423 (2011).
11. T. B. Britton, F. P. E. Dunne, A. J. Wilkinson, On the mechanistic basis of deformation at the microscale in hexagonal close-packed metals. *Proc. R. Soc. A Math. Phys. Eng. Sci.* **471**, 20140881 (2015).
12. K. Firm, R. Boyer, G. Welsch, *Materials Properties Handbook: Titanium Alloys* (ASM International, 1994).
13. D. J. Truax, C. J. McMahon Jr., Plastic behavior of titanium-aluminum alloys. *Mater. Sci. Eng.* **13**, 125–139 (1974).
14. M. J. Blackburn, J. C. C. Williams, Strength, deformation modes and fracture in titanium-aluminum alloys (Yield strength, deformation modes and fracture characteristics of Ti-Al alloys, examining strength and fracture characteristics as function of structure and chemical composition). *Asm. Trans. Quart.* **62**, 398–409 (1969).
15. H. Conrad, On the strengthening of titanium by aluminum. *Scr. Metall.* **7**, 509–512 (1973).
16. T. Neeraj, D.-H. Holc, G. S. Daehn, M. J. Mills, Phenomenological and microstructural analysis of room temperature creep in titanium alloys. *Acta Mater.* **48**, 1225–1238 (2000).
17. T. Neeraj, M. J. Mills, Short-range order (SRO) and its effect on the primary creep behavior of a Ti–6wt.%Al alloy. *Mater. Sci. Eng. A* **319–321**, 415–419 (2001).
18. T. Neeraj, M. J. Mills, Observation and analysis of weak-fringing faults in ti-6 wt% al. *Philos. Mag.* **82**, 779–802 (2002).
19. A. Fitzner, D. G. LeoPrakash, J. Q. Fonseca, M. Thomas, S.-Y. Zhang, J. Kelleher, P. Manuel, M. Preuss, The effect of aluminium on twinning in binary alpha-titanium. *Acta Mater.* **103**, 341–351 (2016).
20. R. Zhang, S. Zhao, C. Ophus, Y. Deng, S. J. Vachhani, B. Ozdol, R. Traylor, K. C. Bustillo, J. W. Morris Jr., D. C. Chrzan, M. D. Asta, A. M. Minor, Direct imaging of short-range order and its relationship to deformation in Ti-6Al. *Sci. Adv.* **5**, eaax2799 (2019).
21. A. van de Walle, M. Asta, First-principles investigation of perfect and diffuse antiphase boundaries in HCP-based Ti-Al alloys. *Metall. Mater. Trans. A Phys. Metall. Mater. Sci.* **33**, 735–741 (2002).
22. H. H. Wu, D. R. Trinkle, Direct diffusion through interpenetrating networks: Oxygen in titanium. *Phys. Rev. Lett.* **107**, 045504 (2011).
23. R. G. Hennig, D. R. Trinkle, J. Bouchet, S. G. Srinivasan, R. C. Albers, J. W. Wilkins, Impurities block the α to ω martensitic transformation in titanium. *Nat. Mater.* **4**, 129–133 (2005).
24. M. A. Bhatia, X. Zhang, M. Azarnoush, G. Lu, K. N. Solanki, Effects of oxygen on prismatic faults in α-Ti: A combined quantum mechanics/molecular mechanics study. *Scr. Mater.* **98**, 32–35 (2015).
25. M. Ghazisaeidi, D. R. Trinkle, Interaction of oxygen interstitials with lattice faults in Ti. *Acta Mater.* **76**, 82–86 (2014).
26. M. I. Baskes, Modified embedded-atom potentials for cubic materials and impurities. *Phy. Rev. B* **46**, 2727–2742 (1992).
27. B. A. Bilby, A. G. Crocker, The theory of the crystallography of deformation twinning. *Proc. R. Soc. London. Ser. A Math. Phys. Sci.* **288**, 240–255 (1965).
28. Y. B. Chun, S. H. Yu, S. L. Semiatin, S. K. Hwang, Effect of deformation twinning on microstructure and texture evolution during cold rolling of CP-titanium. *Mater. Sci. Eng. A* **398**, 209–219 (2005).
29. A. Serra, D. J. Bacon, A new model for {1012} twin growth in hcp metals. *Philos. Mag.* **73**, 333–343 (1996).
30. S. G. Song, G. T. Gray III, Structural interpretation of the nucleation and growth of deformation twins in Zr and Ti—II. Tem study of twin morphology and defect reactions during twinning. *Acta Metall. Mater.* **43**, 2339–2350 (1995).
31. F. Xu, X. Zhang, H. Ni, Q. Liu, {11$\bar{2}$4} deformation twinning in pure Ti during dynamic plastic deformation. *Mater. Sci. Eng. A* **541**, 190–195 (2012).
32. S. J. Lainé, K. M. Knowles, {11$\bar{2}$4} deformation twinning in commercial purity titanium at room temperature. *Philos. Mag.* **95**, 2153–2166 (2015).
33. S. Mullins, B. M. Patchett, Deformation microstructures in titanium sheet metal. *Metall. Trans. A* **12**, 853–863 (1981).
34. S. Ishiyama, S. Hanada, O. Izumi, Orientation dependence of twinning in commercially pure titanium. *J. Jpn. Inst. Met.* **54**, 976–984 (1990).
35. N. M. Madhava, R. W. Armstrong, Discontinuous twinning of titanium at 4.2 K. *Met. Trans.* **5**, 1517–1519 (1974).
36. M. S. Hooshmand, C. Niu, D. R. Trinkle, M. Ghazisaeidi, First-principles prediction of oxygen diffusivity near the (10$\bar{1}$2) twin boundary in titanium. *Acta Mater.* **156**, 11–19 (2018).
37. M. S. Hooshmand, M. Ghazisaeidi, Solute/twin boundary interaction as a new atomic-scale mechanism for dynamic strain aging. *Acta Mater.* **188**, 711–719 (2020).

38. G. Lu, N. Kioussis, V. V. Bulatov, E. Kaxiras, Generalized-stacking-fault energy surface and dislocation properties of aluminum. *Phys. Rev. B* **62**, 3099–3108 (2000).
39. M. S. Daw, Elasticity effects in electronic structure calculations with periodic boundary conditions. *Comput. Mater. Sci.* **38**, 293–297 (2006).
40. N. Lehto, S. Öberg, Effects of dislocation interactions: Application to the period-doubled core of the 90° partial in silicon. *Phys. Rev. Lett.* **80**, 5568–5571 (1998).
41. W. Cai, V. V. Bulatob, J. P. Chang, J. Li, S. Yip, Periodic image effects in dislocation modelling. *Philos. Mag.* **83**, 539–567 (2003).
42. G. Kresse, J. Furthmüller, Efficiency of *ab*-initio total energy calculations for metals and semiconductors using a plane-wave basis set. *Comput. Mater. Sci.* **6**, 15–50 (1996).
43. G. Kresse, J. Furthmüller, Efficiency iterative schemes for ab initio total-energy calculations using a plane-wave basis set. *Phys. Rev. B* **54**, 11169–11186 (1996).
44. J. P. Perdew, K. Burke, M. Ernzerhof, Generalized gradient approximation made simple. *Phys. Rev. Lett.* **77**, 3965–3868 (1997).
45. M. Methfessel, A. T. Paxton, High-precision sampling for Brillouin-zone integration in metals. *Phys. Rev. B* **40**, 3616–3621 (1989).
46. P. Wisesa, K. A. McGill, T. Mueller, Efficient generation of generalized Monkhorst-Pack grids through the use of informatics. *Phys. Rev. B* **93**, 115109 (2016).
47. M. Poschmann, M. Asta, D. C. Chrzan, Convergence of calculated dislocation core structures in hexagonal close packed titanium. *Model. Simul. Mater. Sci. Eng.* **26**, 014003 (2018).
48. S. Plimpton, Fast parallel algorithms for short-range molecular dynamics. *J. Comput. Phys.* **117**, 1–19 (1995).
49. R. G. Hennig, T. J. Lenosky, D. R. Trinkle, S. P. Rudin, J. W. Wilkins, Classical potential describes martensite phase transformations between the α, β, and ω titanium phases. *Phys. Rev. B* **78**, 054121 (2008).
50. P. C. Zhang, D. R. Trinkle, A modified embedded atom method potential for interstitial oxygen in titanium. *Comput. Mater. Sci.* **124**, 204–210 (2016).
51. N. Chaari, D. Rodney, E. Clouet, Oxygen-dislocation interaction in titanium from first principles. *Scr. Mater.* **162**, 200–203 (2019).
52. A. J. E. Foreman, M. J. Makin, Dislocation movement through random arrays of obstacles. *Philos. Mag.* **14**, 911–924 (1966).
53. A. Stukowski, K. Albe, Extracting dislocations and non-dislocation crystal defects from atomistic simulation data. *Model. Simul. Mater. Sci. Eng.* **18**, 085001 (2010).
54. A. Stukowski, Visualization and analysis of atomistic simulation data with OVITO–the Open visualization tool. *Model. Simul. Mater. Sci. Eng.* **18**, 015012 (2010).
55. A. Stukowski, Structure identification methods for atomistic simulations of crystalline materials. *Model. Simul. Mater. Sci. Eng.* **20**, 045021 (2012).
56. A.G. Khachaturian, *Theory of Structural Transformations in Solids* (Dover, 1983).
57. K. Huang, On the atomic theory of elasticity. *Proc. R. Soc. Lond. A* **203**, 178–194 (1950).
58. M. Born, K. Huang, *Dynamic Theory of Crystal Lattices* (Oxford, 1954).

Acknowledgments: We would like to thank TIMET for the production of the model alloys, and D. Rugg from Rolls Royce, UK, for the helpful discussions on the project. **Funding:** We gratefully acknowledge funding from the U.S. Office of Naval Research under grant nos. N00014-16-1-2304 and N0014-19-1-2376. Work at the Molecular Foundry was supported by the Office of Science, Office of Basic Energy Sciences, of the U.S. Department of Energy under contract no. DE-AC02-05CH11231. Computational resources were provided by the Berkeley Research Computing program at the University of California, Berkeley. This work made use of computational resources provided by the Extreme Science and Engineering Discovery Environment (XSEDE), which is supported by the National Science Foundation under grant no. ACI-1053575. **Author contributions:** Y.C., R.Z., M.P., and A.M.M. prepared the manuscript, which was reviewed and edited by all authors; Y.C., R.Z., and S.Z. conducted the tensile tests; Y.C. and R.Z. analyzed the tensile data; Y.C. conducted the fracture tomography characterization; Y.C., R.Z., and S.Z. conducted the TEM experiments; Y.C. and S.Z. conducted the EBSD experiments and twin boundary analysis; M.P., E.R., D.C.C., and M.A. conducted the theoretical calculations on dislocation oxygen interactions; D.L.O. and M.A. conducted the calculation of short-range order; M.S.H. and M.A. conducted the simulation of deformation twins. Project administration, supervision, and funding acquisition were performed by M.A., D.C.C., J.W.M.J., and A.M.M. **Competing interests:** The authors declare that they have no competing interests. **Data and materials availability:** All data needed to evaluate the conclusions in the paper are present in the paper and/or the Supplementary Materials. Additional data related to this paper may be requested from the authors.

Submitted 23 April 2020
Accepted 10 September 2020
Published 23 October 2020
10.1126/sciadv.abc4060

Citation: Y. Chong, M. Poschmann, R. Zhang, S. Zhao, M. S. Hooshmand, E. Rothchild, D. L. Olmsted, J. W. Morris Jr., D. C. Chrzan, M. Asta, A. M. Minor, Mechanistic basis of oxygen sensitivity in titanium. *Sci. Adv.* **6**, eabc4060 (2020).